RESEARCH ARTICLE

Sparse 3D reconstructions in Electrical Impedance Tomography using real data

Matthias Gehre[a] Tobias Kluth[b] Cristiana Sebu [c*] Peter Maass[a]

[a] *Center for Industrial Mathematics, University of Bremen, D-28334 Bremen, Germany;*
[b] *Cognitive Neuroinformatics, University of Bremen, D-28334 Bremen, Germany;*
[c] *Department of Mechanical Engineering and Mathematical Sciences, Oxford Brookes University, Oxford OX33 1HX, UK*

We present a 3D reconstruction algorithm with sparsity constraints for Electrical Impedance Tomography (EIT). EIT is the inverse problem of determining the distribution of conductivity in the interior of an object from simultaneous measurements of currents and voltages on its boundary. The feasibility of the sparsity reconstruction approach is tested with real data obtained from a new planar EIT device developed at the Institut für Physik, Johannes Gutenberg Universität, Mainz, Germany. The complete electrode model is adapted for the given device to handle incomplete measurements and the inhomogeneities of the conductivity are *a priori* assumed to be sparse with respect to a certain basis. This prior information is incorporated into a Tikhonov-type functional by including a sparsity-promoting ℓ^1-regularization term. The functional is minimized with an iterative soft shrinkage-type algorithm.

Key words: electrical impedance tomography, sparsity reconstruction, Tikhonov regularization

1. Introduction

Electrical Impedance Tomography (EIT) is a non-destructive, low-cost and portable imaging technique developed to reconstruct the conductivity distribution in the interior of an object. The technique is also non-invasive since only electrical measurements of currents and voltages on the boundary are performed. EIT can therefore be used as an imaging method in industry (e.g. detection of cracks in concrete [1] or imaging of fluid flows and their mixing in pipes [2]), geophysics (e.g. detection of deposits and reconstruction of structures under the ground from measumements on the surface of the Earth [3]) and medicine (e.g. breast cancer detection and lung function monitoring [4]).

The inverse conductivity problem is a nonlinear parameter identification problem for differential equations which is severely ill-posed in the Hadamard sense. Therefore, it requires an efficient, stable, and accurate mathematical and numerical treatment. A wide range of reconstructions algorithms from noisy measurements have been proposed over the years [5–15]. Many of these algorithms are based on minimizing a certain (regularized) least-square functional, i.e. the squared ℓ^2-norm of the difference between measured potentials and computed potentials for an estimated distribution of conductivity. Due to the ill-posedness of the problem, different regularization methods were applied and their suitability investigated.

*Corresponding author. Email: csebu@brookes.ac.uk

Figure 1. The sensing head.

Examples include smoothness regularization [9, 12, 16], total variation [8, 10, 13] or regularization by the Mumford-Shah functional [11]. Despite all these efforts, the quality of reconstructions is still modest when compared to other (non-diffuse) imaging modalities.

However, when the object under consideration exhibits sparse features, i.e. it consists of an ordinary (e.g. constant) background conductivity and a few inclusions which have rather simple mathematical descriptions, the use of an ℓ^1 norm in the regularization term could enhance the accuracy of the EIT reconstructions. Since the pioneering work on sparsity constraints for least-squares problems with a linear operator [17], substantial progress has been made especially in developing efficient algorithms with ℓ^1 priors for solving both linear and non-linear inverse problems [18–22]. Recently, this so-called sparsity regularization has been successfully applied to two-dimensional EIT [23, 24].

In this paper we use a sparsity algorithm to obtain three-dimensional reconstructions from real data collected using a new planar electrical impedance tomography device developed at the Institut für Physik, Johannes Universität, Mainz, Germany. The latest Mainz tomograph was designed mainly for breast cancer detection and is similar to the one described in [25, 26]. Its sensing head consists of a supporting plastic plate with fixed electrodes, namely 12 large outer (active) electrodes where the external currents are injected, and a set of 54 point-like high-impedance inner(passive) electrodes where the induced potentials are measured (see Figure 1). To avoid any problems due to the unknown contact impedance, the potentials are not measured at the outer electrodes. At the inner electrodes very high impedance voltage measurements are taken and the problem of contact impedance does not arise. In almost all previous EIT experimental setups the same electrodes were used for current injection and voltage measurement. The excitation current was injected (extracted) at one pair of electrodes at each time and the resulting voltage was measured at all or some of the remaining electrodes, e.g. [4, 24]. The novelty of the device, and hence of the reconstruction method proposed, consists exactly in the distinct use of active and passive electrodes. The active electrodes are used only for current injection while the passive electrodes only for voltage measurements.

The paper is structured as follows. The complete electrode model which we use as a mathematical model for the data formation/acquisition process is reviewed and adapted to the planar EIT device developed in Mainz in section 2. The reconstruction algorithm is described in section 3 and we indicate all the specific issues related to its implementation. Finally, in section 4, we describe the measurement device and the experimental setup, present the numerical reconstructions from real

data and evaluate the proposed method.

2. Complete electrode model with incomplete measurements

Due to the ill-posed nature of the considered problem, accurate description of the physical processes is very important. Different electrode models for EIT have been proposed and studied in [27] and their accuracy was compared. The most accurate model turned out to be the so-called complete electrode model (CEM), which includes various physical effects into the modelling. We briefly review this model following the description in [27] and adapt it to the planar data collection EIT device developed in Mainz.

Let Ω be the conductive object under consideration, and $\Gamma = \partial\Omega$ be its surface (boundary).The experimental procedure of performing potential measurements is as follows. First, a set of L electrodes is placed on the surface of the object. Then, an input current is applied to the L electrodes and the resulting potentials are measured at a number M of electrodes. This procedure is repeated several times with different currents patterns. The complete electrode model takes into account distinct features of the EIT experiment, i.e. the discrete nature of the electrodes, effect of the contact impedance and the shunting effect of the electrodes, and it is now regarded as the standard electrode model in medical applications. In contrast to the original complete electrode model where $M = L$, the potential is not measured at all L electrodes, but only at a subset of M of electrodes ($M \leq L$).

The CEM is of the form

$$\begin{cases} -\nabla \cdot (\sigma \nabla u) = 0 & \text{in } \Omega, \\ u + z_l \sigma \frac{\partial u}{\partial n} = U_l & \text{on } e_l, l = 1, \ldots, L, \\ \int_{e_l} \sigma \frac{\partial u}{\partial n} ds = I_l & \text{for } l = 1, \ldots, L, \\ \sigma \frac{\partial u}{\partial n} = 0 & \text{on } \Gamma \setminus \cup_{l=1}^{L} e_l, \end{cases} \tag{1}$$

where σ is the electrical conductivity, $u \in H^1(\Omega)$ is the electric potential, $\{e_l\}_{l=1}^{L} \subset \Gamma$ denote the surfaces under the electrodes and n is the unit outward normal to the boundary Γ. Moreover, $U_l, I_l \in \mathbb{R}, l = 1, \ldots, L$ are the electrode potentials and currents, respectively. The currents have to satisfy the charge conservation law, and hence $\sum_{l=1}^{L} I_l = 0$. For uniqueness, the ground potential has to be fixed; this is achieved for example by requiring $\sum_{l=1}^{L} U_l = 0$. We denote the vectors consisting of electrode potentials and currents by U and I, i.e. $U = (U_1, U_2, \ldots, U_L)^{\mathrm{T}} \in \mathbb{R}^L_\Sigma$ and $I = (I_1, I_2, \ldots, I_L)^{\mathrm{T}} \in \mathbb{R}^L_\Sigma$, where $\mathbb{R}^L_\Sigma = \{x \in \mathbb{R}^L : \sum_{l=1}^{L} x_l = 0\}$.

The second equation in system of equations (1) models the contact impedance effect. When injecting electrical currents into the object, a thin layer with high resistivity forms at the electrode-electrolyte interface due to certain electrochemical processes, which causes the potential values to drop at the electrodes according to Ohm's law. Note that the left-hand side $u + z_l \sigma \frac{\partial u}{\partial n}$ of the second equation is a function defined on each electrode, whereas the right-hand side U_l is a scalar. This is due to the shunting effect: the electrodes are modelled as perfect conductors and the potential is therefore constant on them. The third equation in (1) reflects the fact that the current injected through each electrode is completely confined to the electrode.

We define the forward operator of the EIT problem by $F(\sigma) : \mathbb{R}^L_\Sigma \to H^1(\Omega) \times \mathbb{R}^L_\Sigma$, $I \mapsto (u, U)$, which is equivalent to solving the above equations. The forward

operator is well-defined, linear and continuous in I [27].

We also define the measurement operator by $\mathcal{M} : H^1(\Omega) \times \mathbb{R}^L_\Sigma \to \mathbb{R}^M$, $(u, U) \mapsto (U_1, \ldots, U_M)^{\mathrm{T}}$ which restricts the tuple (u, U) to the measurable potentials. One EIT experiment then corresponds to the composition $U = \mathcal{M}F(\sigma)I$. For the device under consideration, it is not possible to inject current into the M potential measuring electrodes, i.e. $I_l = 0$ for $l = 1, \ldots, M$. Thus, the contact impedance effect on the electrode potentials U_l becomes negligible and there is no need to approximate the contact impedances z_l correctly.

Unfortunately, the analytical solution of (1) is usually intractable. Thus we employ a finite element method, see [9, 14] for details. To this end, we exploit the weak formulation of (1), which reads

$$\int_\Omega \sigma \nabla u \cdot \nabla v \, dx + \sum_{l=1}^{L} \frac{1}{z_l} \int_{e_l} (U_l - u)(V_l - v) \, dS = \sum_{l=1}^{L} I_l V_l$$

for all $v \in H^1(\Omega), V \in \mathbb{R}^L_\Sigma$.

Choosing a basis $\{\phi_i\}_{i=1,\ldots,N}$ of a suitable finite element space, one can replace u by its basis expansion $u = \sum_{i=1}^{N} u_i \phi_i$ and test against every $v = \phi_i$ for $i = 1, \ldots, N$ to arrive, in matrix form, at the linear system

$$\underbrace{\begin{bmatrix} \mathcal{K}^0 + \mathcal{K}^r & \mathcal{K}^b \\ (\mathcal{K}^b)^{\mathrm{T}} & \mathcal{K}^d \end{bmatrix}}_{A} \begin{bmatrix} u \\ U \end{bmatrix} = \begin{bmatrix} 0 \\ I \end{bmatrix} \tag{2}$$

with

$$\begin{aligned}
\mathcal{K}^0_{ij} &:= \int_\Omega \sigma \nabla \phi_i \cdot \nabla \phi_j \, \mathrm{d}x && i, j = 1, \ldots, N \\
\mathcal{K}^r_{ij} &:= \sum_{l=1}^{L} \frac{1}{z_l} \int_{e_l} \phi_i \phi_j \, \mathrm{d}S && i, j = 1, \ldots, N \\
\mathcal{K}^b_{ij} &:= -\frac{1}{z_j} \int_{e_i} \phi_i \, \mathrm{d}S && i = 1, \ldots, N \text{ and } j = 1, \ldots, L \\
\mathcal{K}^d_{ii} &:= \frac{1}{z_i} \int_{e_i} 1 \, \mathrm{d}S && i = 1, \ldots, L
\end{aligned}$$

and $u = (u_1, \ldots, u_N)^T$. The matrix A is symmetric, positive semi-definite and sparse. It is singular, because the condition $U \in \mathbb{R}^L_\Sigma$ has not been accounted for yet, and so every constant offset of one solution is another solution to that matrix equation. In [14] it is suggested to add the row

$$[\underbrace{0 \cdots 0}_{N \text{ times}} \underbrace{1 \cdots 1}_{L \text{ times}}]$$

to A and at the same time extend the right-hand side vector of the linear system (2) by an additional zero entry. Unfortunately, this destroys symmetry and squareness of the original matrix, which in turn has bad influence on stability and performance. We follow [10], where U is expanded in a basis of $\mathbb{R}^L_\Sigma$ instead of $\mathbb{R}^L$ to enforce the

zero sum condition. Note that this only affects the matrices $\mathcal{K}^b$ and $\mathcal{K}^d$, which are of small dimensions, thus the transformation can be carried out inexpensively.

3. Tikhonov approach

The EIT inverse problem is to estimate an unknown conductivity $\sigma^\dagger$ from a finite set of noisy potential data U^δ. It suffers from severe ill-posedness and must, as a result, be regularized. We use the very popular Tikhonov regularization, which defines an approximation to the unknown conductivity for the data set (I, U^δ) as the minimizer σ^* of

$$\sigma^* = \arg\min_{\sigma\in\mathcal{A}} \left\{ J_\alpha(\sigma) = \underbrace{\tfrac{1}{2}\|\mathcal{M}F(\sigma)I - U^\delta\|^2}_{D(\sigma)} + \alpha R(\sigma) \right\},$$

where $R(\sigma)$ is a regularization functional, $D(\sigma)$ is the discrepancy term and $U^\delta = (U_1^\delta, \ldots, U_M^\delta)$ denotes the noisy potential measurements. From elliptic regularity theory, the admissible set $\mathcal{A}$ is restricted to a positive, uniformly bounded subset of $L^\infty(\Omega)$. To this end, we define

$$\mathcal{A} = \{\sigma \in L^\infty(\Omega) : 0 < c_0 \leq \sigma \leq c_1 \text{ a.e. in } \Omega\},$$

where c_0 and c_1 are known positive constants.

This formulation can be modified in a straightforward way to incorporate multiple data sets $\{(I^k, U^{\delta k})\}_{k=1}^K$ by modifying the discrepancy $D(\sigma)$ to

$$D(\sigma) = \tfrac{1}{2}\sum_{k=1}^{K} \|\mathcal{M}F(\sigma)I^k - U^{\delta k}\|^2.$$

However, for notational simplicity, we consider only one single data set (I, U^δ).

The scalar parameter α denotes the regularization parameter, which balances between the discrepancy term and the regularization functional. It incorporates a priori information about properties of the solution and the noise level.

There is a variety of regularization functionals to choose from, each of them suitable for a certain type of *a priori* knowledge available of the true conductivity $\sigma^\dagger$. Here, we consider conductivities which consist of a known or simple (e.g. constant) background plus some inclusions with small support with respect to a certain basis. The natural choice of regularization functional for this kind of a priori knowledge is an ℓ^p norm

$$\|x\|_{\ell^p}^p = \sum_n |\langle x, b_n\rangle|^p$$

for $p \leq 1$ with respect to a certain basis $\{b_n\}$. Popular choices for bases include the pixel basis, the finite element basis or wavelet bases.

The l_0-norm corresponds to the cardinality of the support, thus is a reasonable measure for smallness of inclusions. Unfortunately, obtaining the minimizer of the NP-hard ℓ^0-regularized problem is computationally unachievable. The ℓ^1-norm, on the other hand, is the closest convex relaxation of the ℓ^0-norm. By virtue of its convexity, it lends itself to tractable algorithms, and serves as an approximation

to the ℓ^0-norm. Hence we define the regularization functional as

$$R(\sigma) = \|\sigma - \sigma_{\text{bg}}\|_{\ell^1}$$

where $\sigma_{\text{bg}} \in H^1(\Omega)$ is the known background conductivity. For a comparison of sparsity regularization to the widely used smoothness regularization on experimental EIT data, see [24].

Algorithms to compute the minimizer of general sparsity-regularized functionals have been discussed in [18, 19, 21]. One of the algorithms under consideration is the iterative soft shrinkage algorithm, which was applied to EIT with the continuum model in [23]. In this paper, we employ a variant of this algorithm from [24]; see Algorithm 1 for a complete description.

Algorithm 1 Sparse reconstruction algorithm

1: Set $\delta\sigma^0 = 0$
2: **for** $j = 1, \ldots, J$ **do**
3: Compute $\sigma^j = \sigma_{\text{bg}} + \delta\sigma^j$;
4: Compute the gradient $D'(\sigma^j)$ by the adjoint method;
5: Compute the smoothed gradient $D'_s(\sigma^j)$;
6: Determine the step size τ_j;
7: Update inhomogeneity by $\delta\sigma^{j+1} = \delta\sigma^j - \tau_j D'_s(\sigma^j)$;
8: Threshold $\delta\sigma^{j+1}$ by $S_{\tau_j \alpha}(\delta\sigma^{j+1})$;
9: Check a stopping criterion.
10: **end for**
11: **output** approximate minimizer $\delta\sigma$ and return $\delta\sigma + \sigma_{\text{bg}}$.

The algorithm iteratively updates an approximation $\delta\sigma$ to the true inclusion $\sigma^* - \sigma_{\text{bg}}$. In each iteration, it first computes the gradient of the discrepancy term (by the adjoint method, see appendix A), then smooths the gradient to increase regularity, updates the conductivity by a gradient descent step with suitable chosen step size, and finally applies a thresholding operator $S_{\tau_j \alpha}$ to enforce sparsity. Special attention has to be paid to the smoothing step and on the choice of suitable stepsize for their crucial influence on stability and performance of the algorithm.

We experienced considerable oscillations and artifacts in the reconstruction when directly using the gradient $D'(\sigma^j)$ to update the inhomogeneity. These numerical difficulties were overcome by introducing the Sobolev gradient (or smoothed gradient), $D'_s(\sigma^j)$, which is defined as the gradient with respect to the H^1-scalar product, i.e

$$\left\langle D'(\sigma^j), h \right\rangle_{L^2(\Omega)} = \left\langle D'_s(\sigma^j), h \right\rangle_{H^1(\Omega)} \text{ for all } h \in H^1(\Omega).$$

Reordering this equation we arrive at the weak formulation for the following linear partial differential equation

$$-\Delta D'_s(\sigma^j) + D'_s(\sigma^j) = D'(\sigma^j) \text{ on } \Omega. \tag{3}$$

One can also introduce a parameter β into equation (3)

$$-\beta\Delta D'_s(\sigma^j) + D'_s(\sigma^j) = D'(\sigma^j) \text{ on } \Omega$$

to control the strenght of smoothing.

To accelerate this inherently slow gradient-descent-type method, we choose an adaptive step size selection rule devised by Barzilai and Borwein [28]. The basic idea is to make the scalar step size mimic the inverse of the Hessian, i.e. to solve

$$\tau^j(\sigma^j - \sigma^{j-1}) \approx D'_s(\sigma^j) - D'_s(\sigma^{j-1})$$

in the least square sense. This approach results in the computational simple formula

$$\tau^j = \frac{\langle \sigma^j - \sigma^{j-1}, D'_s(\sigma^j) - D'_s(\sigma^{j-1}) \rangle}{\langle \sigma^j - \sigma^{j-1}, \sigma^j - \sigma^{j-1} \rangle}.$$

Algorithms based on Barzilai-Borwein are sometimes implemented in an unconstrained fashion where the objective value $J(\sigma)$ does not have to decrease at all, but their convergence is hard to study. On the other hand, the non-monotony (with $\mathfrak{M} > 0$) is characteristic for Barzilai-Borwein and necessary for fast convergence. We follow [22] by enforcing a 'weak monotony", i.e. after we have obtained a candidate step size by Barzilai-Borwein's rule, it is only accepted if it yields a lower value in the objective function than any of the last $\mathfrak{M}$ iterates, where $\mathfrak{M}$ is a fixed parameter. If a candidate step size is rejected, it is halved and the criterion is evaluated again.

The second last step of algorithm **1** applies the soft shrinkage (or soft thresholding) operator $S_{\tau_j \alpha}$ to the result of the gradient descent step. The soft shrinkage operator is defined componentwise by

$$(S_\alpha(x))_i = \begin{cases} (|x_i| - \alpha)\,\mathrm{sign}(x_i) & \text{if } |x_i| > \alpha \\ 0 & \text{otherwise} \end{cases}$$

acting on the coeffiecients x_i of the basis expansion of x. It sets all small (smaller than α) coefficients to zero and shrinks all other by α towards zero.

The first five steps can be viewed as minimizing the discrepancy $D(\sigma)$, and the application of the soft-shrinkage operator $S_{\tau_j \alpha}$ takes care of the minimization of the regularization functional $R(\sigma)$ by enforcing sparsity. It has been shown in [18] that under some conditions this iterated soft shrinkage algorithm will converge to a minimizer of the functional $J(\sigma)$.

4. Experimental setup and numerical reconstructions from real data

The Mainz tomograph has three parts: a planar sensing head of circular geometry, an electronic device to apply the current patterns and to measure the electric potentials, and a computer for image reconstruction. More technical details of the Mainz EIT system can be found in [29]. The sensing head has a fixed geometry. There are $L = 66$ electrodes fixed on a supporting plastic circular plate of diameter 10 cm and their positions are exactly known. The $M = 54$ passive electrodes where the potentials are measured are very small (2 mm-diameter electrodes), practically no current is drawn and they are placed in a hexagonal pattern (electrodes labeled 13 to 66 in Figure 2). The 12 large active electrodes where the currents is injected have diameters of 10 mm and their centers are placed on a circle of radius $R = 4.4$ cm (electrodes labeled 1 to 12 in Figure 2).

The experimental data were collected by placing the sensing head at the bottom of a cylindrical tank of the same diameter as the sensing head which was filled with a conducting liquid (salt water). The water level in the tank was approximately 8 cm. Objects made out of different materials were immersed in the liquid at different

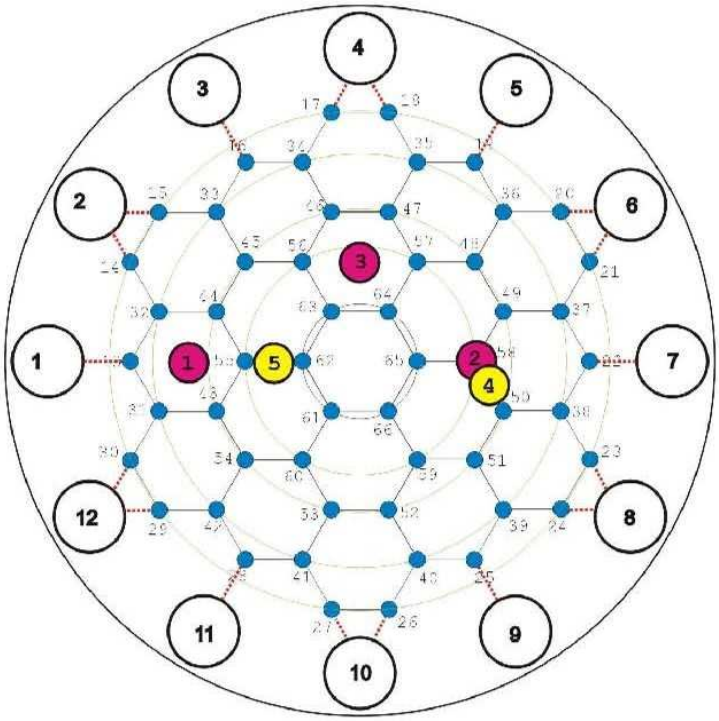

Figure 2. Layout of the electrode array of the Mainz EIT device. The small circles labeled from 1 to 12 show the outer electrodes for current injection. The position of the 54 inner electrodes for potential measurements are drawn as thick points (marked in blue). The network is used as a model of the measurement area. The positions 1, 2, and 3 (marked in red) indicate the places above the sensing head where metallic objects were immersed in conducting liquid, while the positions 4 and 5 (marked in yellow) indicate the places where an agar phantom was placed.

distances from the sensing head, see Figure 2. Metallic cyllindrical objects, M20 and M15, which have diameters and heights equal to 20 mm and 15 mm, respectively, were placed at positions 1, 2 and 3. A lower contrast inclusion, i.e. a cubic agar phantom of side equal to 20 mm, was placed at positions 4 and 5. Although the distances from the sensing head were accurately measured, the actual positions of the immersed objects might differ slightly from from those indicated in Figure 2 due to technical reasons. Data were collected for only $K = 10$ varying-frequency patterns of the input current:

$$I^{(\alpha)}(\theta_s) = \begin{cases} I_0^{(\alpha)} \cos(\alpha\theta_s), & \alpha = 1, \ldots, 5, \\ I_0^{(\alpha)} \sin((\alpha - 5)\theta_s), & \alpha = 6, \ldots, 10, \end{cases} \tag{4}$$

where $\theta_s = \frac{\pi s}{6}$, $s = 1, \ldots, 12$, is the angular position of the centers of the current electrodes.

Note that the experimental setup and the data collection process are different from those presented in [24] where electrical measurements were performed at the lateral surface of the tank, and hence reconstructions of two-dimensional conductivities were obtained. In this case electrical measurements were performed solely at the bottom of the tank and we reconstruct three-dimensional conductivity distributions.

In the numerical reconstructions, the sensing head is considered to be at height $z = 0$ mm and the tank extends downwards to $z = -2, -6, \ldots$ mm. The volume was approximated by a tetrahedral mesh of 42496 elements and a piecewise linear finite element space was used for both the potential u and the conductivity σ. We also considered sparsity with respect to that finite element basis. The reconstructions

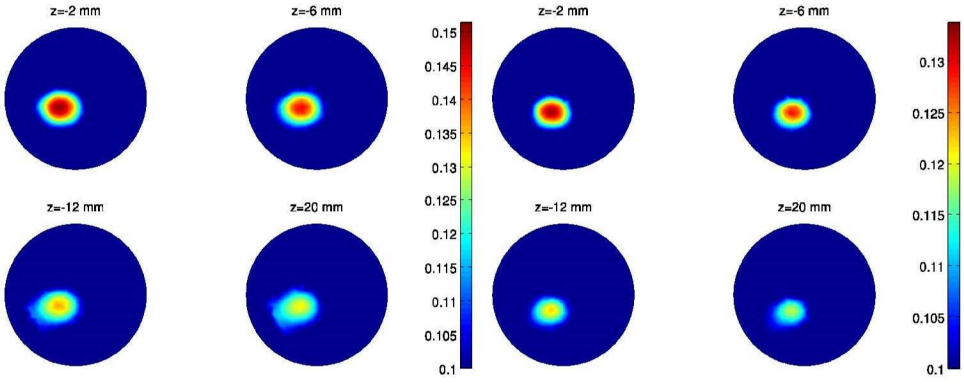

(a) $z = -2$ mm (b) $z = -10$ mm

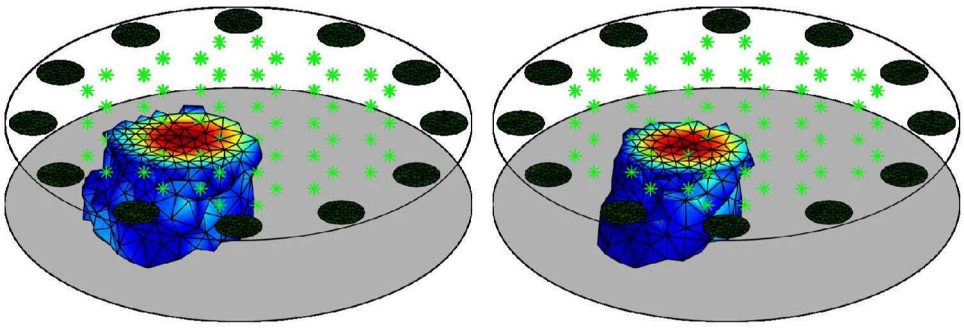

(c) $z = -2$ mm (d) $z = -10$ mm

Figure 3. Conductivity reconstructions for the agar phantom placed at position 5 and at different distances below the sensing head: (a) and (c) 2 mm; (b) and (d) 5 mm. (a) and (b): cross sections of conductivity reconstructions; (c) and (d): three-dimensional views of the conductivity reconstructions.

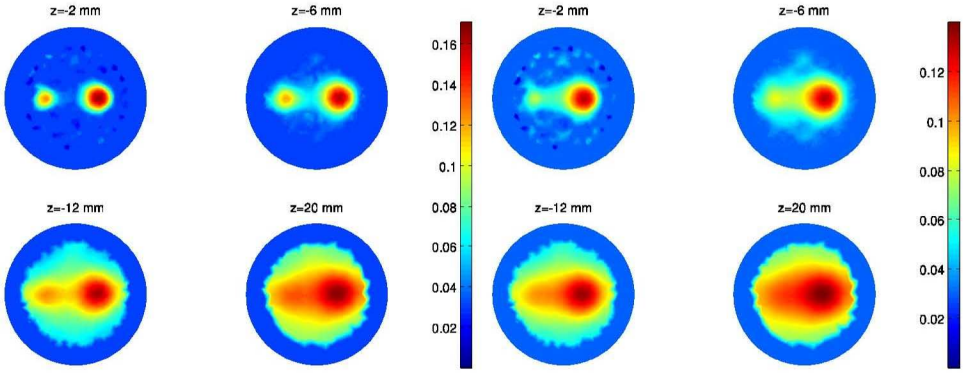

(a) $z = -2$ mm (b) $z = -5$ mm

Figure 4. Cross sections of conductivity reconstruction for M15 at position 1 and M20 at position 2. The inclusion is (a) 2 mm and (b) 5 mm below the sensing head.

took about 8 minutes on a off-the-shelf 2.6 GHz dual-core laptop.

In Figure 3, we present reconstructions for the the agar-phantom placed at position 5 and at two different depths (i.e. two different distances to the sensing head). The conductivity reconstructions look quite similar. They localize the inclusion very well in the x, y-plane confirming that the currents penetrate deep enough. As expected, the planar sensing head cannot provide information about the exact depth and height of the inclusion. Since similar results were obtained for an agar phantom placed at position 4, we decided not to include those in this paper.

Figure 4 shows the conductivity reconstructions for two metallic objects M15 and M20 placed at positions 1 and 2, respectively, and at two different distances

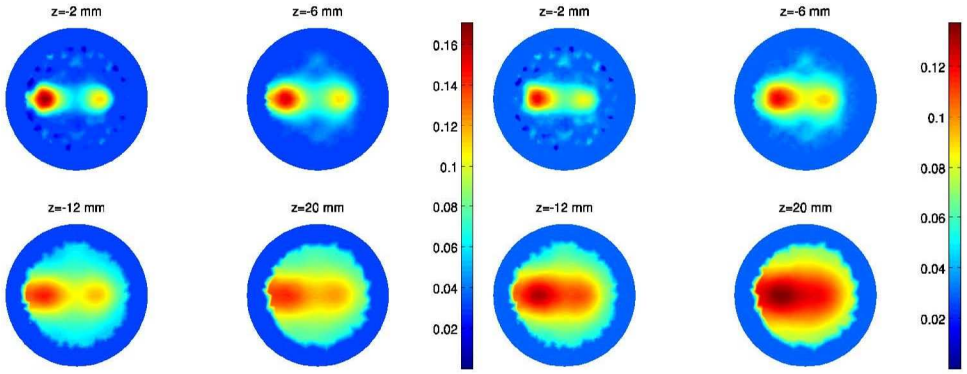

(a) $z = -2$ mm (b) $z = -5$ mm

Figure 5. Cross sections of conductivity reconstruction for M15 at position 2 and M20 at position 1. The inclusion is (a) 2 mm and (b) 5 mm below the sensing head.

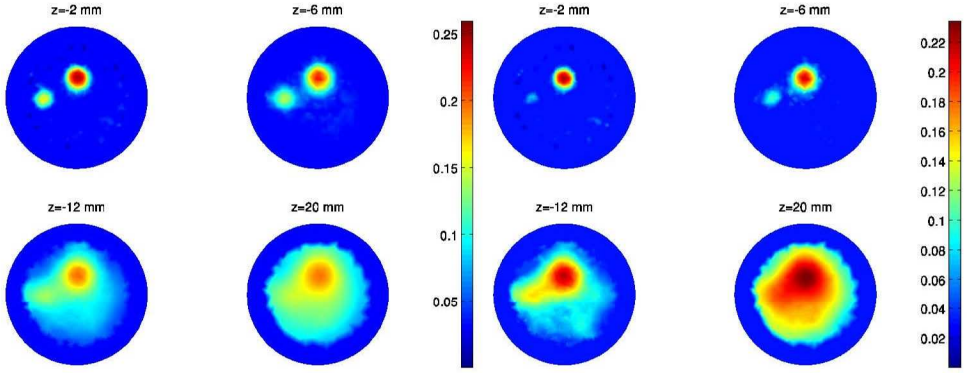

(a) $z = -2$ mm (b) $z = -5$ mm

Figure 6. Cross sections of conductivity reconstruction for M15 at position 1 and M20 at position 3. The inclusion is (a) 2mm and (b) 5mm below the sensing head.

from the sensing head, 2 mm and 5 mm. In figure 6 we present conductivity reconstructions for the same two metallic objects whose positions were swapped. All reconstructions give good localizations of the inclusions. In the experiments with inclusions at depth 5 mm, the separation is worse and the smaller inclusion seems to be shielded by the bigger inclusion. This time the reconstructions contain some oscillations near the electrodes (see cross section at $z = -2$ mm in Figure 6 (b)) which are due to the ill-posed nature of the problem.

Figure 6 shows the reconstructions obtained for the same metallic inclusions placed at different positions, i.e. M15 placed at position 1 and M20 placed at position 3. We observe the same features of the reconstructions as before: good localizations in the x, y-plane and a nice separation of the different inclusions.

5. Conclusions

We applied a sparsity enforcing reconstruction method using the complete electrode model to a new planar EIT device developed in Mainz, Germany. The reconstructions show that objects placed into the tank at various positions and distances from the sensing head could be detected and their positions in x, y-plane recovered. As expected, in the data collected by the Mainz tomograph there is little information about the depth and the heights of the inclusions. Future work includes evaluation of various choice rules for the regularization parameter α for the specific inverse

problem presented here, reconstructions obtained from clinical data and investigations of whether both conductivity and permitivity reconstructions obtained from real data at differernt frequencies of the applied current improve the specificity of breast tumour detections.

Acknowledgements

We would like to thank Professor Karl Schilcher, Professor Hubert Spisberger and Dr Heinz Georgi from the Institut für Physik, Johannes Gutenberg Universität, Mainz, Germany, for providing us the real data collected using the latest planar EIT device designed by their research group. Without their generosity and support of any scientic progress which might lead to breakthroughs for detecting breast cancer by means of EIT, this work would not have been possible. We would also like to thank Dr Bangti Jin for his valuable comments in the preparation of the manuscript.

References

[1] K. Karhunen, A. Seppnen, A. Lehikoinen, P.J. Monteiro, and J.P. Kaipio, *Electrical Resistance Tomography imaging of concrete*, Cement and Concrete Research 40 (2010), pp. 137 – 145.
[2] F. Dickin and M. Wang, *Electrical resistance tomography for process applications*, Measurement Science and Technology 7 (1996), p. 247.
[3] A. Lehikoinen, S. Finsterle, A. Voutilainen, L.M. Heikkinen, M. Vauhkonen, and J.P. Kaipio, *Approximation errors and truncation of computational domains with application to geophysical tomography*, Inverse Probl. Imaging 1 (2007), pp. 371–389.
[4] D.S. Holder (ed.) *Electrical Impedance Tomography: Methods, History and Applications*, Series in Medical Physics and Biomedical Engineering Institute of Physics Publishing, Bristol, 2004.
[5] D.C. Barber and B.H. Brown, *Applied potential tomography*, J. Phys. E: Sci. Instrum. 17 (1984), pp. 723–733.
[6] T.J. Yorkey, J.G. Webster, and W.J. Tompkins, *Comparing reconstruction algorithms for electrical impedance tomography*, IEEE Trans. Biomed. Eng. 34 (1987), pp. 843–852.
[7] M. Cheney, D. Isaacson, J.C. Newell, S. Simske, and J. Goble, *NOSER: An algorithm for solving the inverse conductivity problem*, Int. J. Imag. Syst. Tech. 2 (1990), pp. 66–75.
[8] D. Dobson and F. Santosa, *An image-enhancement technique for Electrical Impedance Tomography*, Inverse Problems 10 (1994), pp. 317–334.
[9] M. Vauhkonen, D. Vadasz, P. Karjalainen, E. Somersalo, and J. Kaipio, *Tikhonov regularization and prior information in electrical impedance tomography*, IEEE Trans. Med. Imag. 17 (1998), pp. 285–293.
[10] J.P. Kaipio, V. Kolehmainen, E. Somersalo, and M. Vauhkonen, *Statistical inversion and Monte Carlo sampling methods in electrical impedance tomography*, Inverse Problems 16 (2000), pp. 1487–1522.
[11] L. Rondi and F. Santosa, *Enhanced electrical impedance tomography via the Mumford-Shah functional*, ESAIM Control Optim. Calc. Var. 6 (2001), pp. 517–538.
[12] M. Lukaschewitsch, P. Maass, and M. Pidcock, *Tikhonov regularization for electrical impedance tomography on unbounded domains*, Inverse Problems 19 (2003), pp. 585–610.
[13] E.T. Chung, T.F. Chan, and X.C. Tai, *Electrical impedance tomography using level set representation and total variational regularization*, J. Comput. Phys. 205 (2005), pp. 357–372.
[14] A. Lechleiter and A. Rieder, *Newton regularizations for impedance tomography: a numerical study*, Inverse Problems 22 (2006), pp. 1967–1987.
[15] A. Kirsch and N. Grinberg, *The Factorization Method for Inverse Problems*, Oxford University Press, Oxford, 2008.
[16] P. Vauhkonen, M. Vauhkonen, T. Savolainen, and J. Kaipio, *Three-dimensional electrical impedance tomography based on the complete electrode model*, IEEE Trans. Biomed. Eng. 46 (1999), pp. 1150–1160.
[17] I. Daubechies, M. Defrise, and C. De Mol, *An iterative thresholding algorithm for linear inverse problems with a sparsity constraint*, Comm. Pure Appl. Math. 57 (2004), pp. 1413–1457.
[18] T. Bonesky, K. Bredies, D.A. Lorenz, and P. Maass, *A generalized conditional gradient method for nonlinear operator equations with sparsity constraints*, Inverse Problems 23 (2007), pp. 2041–2058.
[19] R. Ramlau and G. Teschke, *A Tikhonov-based projection iteration for nonlinear ill-posed problems with sparsity constraints*, Numer. Math. 104 (2006), pp. 177–203.
[20] D.A. Lorenz, *Convergence rates and source conditions for Tikhonov regularization with sparsity constraints*, J. Inverse Ill-Posed Probl. 16 (2008), pp. 463–478.
[21] K. Bredies, D.A. Lorenz, and P. Maass, *A generalized conditional gradient method and its connection to an iterative shrinkage method*, Comput. Optim. Appl. 42 (2009), pp. 173–193.
[22] S.J. Wright, R.D. Nowak, and M. Figueiredo, *Sparse reconstruction by separable approximation*, IEEE Trans. Signal Process. 57 (2009), pp. 2479–2493.
[23] B. Jin, T. Khan, and P. Maass, *A reconstruction algorithm for electrical impedance tomography based on sparsity regularization*; Int. J. Numer. Methods in Engng., 89 (2012), pp. 337–353.

[24] M. Gehre, T. Kluth, A. Lipponen, B. Jin, A. Seppänen, J.P. Kaipio, and P. Maass, *Sparsity reconstruction in electrical impedance tomography: an experimental evaluation*, J. Comput. Appl. Math. 236 (2012), pp. 2126–2136.
[25] M. Azzouz, M. Hanke, C. Oesterlein, and K. Schilcher, *The factorization method for electrical impedance tomography data from a new planar device*, Int. J. Biomedical Imaging 2007 (2007), 7 pages, Article ID 83016.
[26] C. Hähnlein, K. Schilcher, C. Sebu, and H. Spiesberger, *Conductivity imaging with interior potential measurements*, Inv. Probl. Sc. Eng. 19(5) (2011), pp. 729–750.
[27] E. Somersalo, M. Cheney, and D. Isaacson, *Existence and uniqueness for electrode models for electric current computed tomography*, SIAM J. Appl. Math. 52 (1992), pp. 1023–1040.
[28] J. Barzilai and J.M. Borwein, *Two-point step size gradient methods*, IMA J. Numer. Anal. 8 (1988), pp. 141–148.
[29] K-H. Georgi, C. Hähnlein, K. Schilcher, H. Spiesberger and C. Sebu, *Conductivity reconstructions using real data from a new planar electrical impedance device*, Inv. Probl. Sc. Eng. (2013). http://dx.doi.org/10.1080/17415977.2012.753441.

Appendix A. Derivation of the gradient formula

Recall that the discrepancy term is given by

$$D(\sigma) = \tfrac{1}{2}\|\mathcal{M}F(\sigma)I - U^\delta\|^2,$$

where $F(\sigma) : \mathbb{R}^L_\Sigma \to H^1(\Omega) \times \mathbb{R}^L_\Sigma, I \mapsto (u, U)$, is the forward operator, $\mathcal{M} : H^1(\Omega) \times \mathbb{R}^L_\Sigma \to \mathbb{R}^M, (u, U) \mapsto (U_1, \ldots, U_M)^{\mathrm{T}}$, is the measurement operator, and U^δ are the measured potentials.

Proposition A.1: *Let $\sigma \in \mathcal{A}$, $\delta\sigma$ compactly supported on Ω such that $\sigma + \delta\sigma \in \mathcal{A}$, $I \in \mathbb{R}^L_\Sigma$, $U^\delta \in \mathbb{R}^M$, $(u, U) = F(\sigma)I$ and $(p, P) \in H^1(\Omega) \times \mathbb{R}^L_\Sigma$ be the solution of*

$$\begin{aligned}&\int_\Omega \sigma \nabla p \cdot \nabla v \,\mathrm{d}x + \sum_{l=1}^{L} \frac{1}{z_l} \int_{e_l} (P_l - p)(V_l - v) ds \\ &\quad = \Big\langle (\mathcal{M}(u, U) - U^\delta), \mathcal{M}(v, V) \Big\rangle_{\mathbb{R}^M} \quad \textit{for all } (v, V) \in H^1(\Omega) \times \mathbb{R}^L_\Sigma\end{aligned}$$

then the L^2-gradient of the functional $D(\sigma) = \frac{1}{2}\|\mathcal{M}F(\sigma)I - U^\delta\|^2$ is given by

$$\nabla D(\sigma) = -\nabla u \cdot \nabla p. \tag{A1}$$

Remark *A1*: In the above notation, $D'(\sigma)$ is the gradient w.r.t. σ; ∇u and ∇p are spatial gradients.

Remark *A2*: For multiple currents $I^1, \ldots, I^K$, the equations becomes

$$D'(\sigma) = -\sum_{k=1}^{K} \nabla u^k \cdot \nabla p^k.$$

where p^k and u^k have been calculated from their respective currents I^k.

Proof: The derivative of $D(\sigma)$ can be rewritten by the chain-rule as

$$D'(\sigma)\delta\sigma = \Big\langle \mathcal{M}(u, U) - U^\delta, \mathcal{M}(u', U') \Big\rangle_{\mathbb{R}^M},$$

where $(u', U') = F'(\sigma)\delta\sigma$. The weak formulation for (p, P) with $(v, V) = (u', U')$ is

$$\int_\Omega \sigma \nabla p \cdot \nabla u' \,\mathrm{d}x + \sum_{l=1}^{L} \frac{1}{z_l} \int_{e_l} (P_l - p)(U_l' - u') \,\mathrm{d}S = \left\langle \mathcal{M}(u, U) - U^\delta, \mathcal{M}(u', U') \right\rangle_{\mathbb{R}^M}$$

and the weak formulation of (u', U') with $(v, V) = (p, P)$ is

$$\int_\Omega \sigma \nabla p \cdot \nabla u' \,\mathrm{d}x + \sum_{l=1}^{L} \frac{1}{z_l} \int_{e_l} (P_l - p)(U_l' - u') \,\mathrm{d}S = -\int_\Omega \delta\sigma \nabla u \cdot \nabla p.$$

Combining the above two equations leads to

$$D'(\sigma)\delta\sigma = -\int_\Omega \delta\sigma \nabla u \cdot \nabla p \,\mathrm{d}x.$$

Hence, using the definition of the L^2-gradient we obtain

$$D'(\sigma)\delta\sigma = \left\langle D'(\sigma), \delta\sigma \right\rangle_{L^2(\Omega)},$$

which concludes the proof. □

This result allows us to compute the gradient of $D(\sigma)$ without the need to evaluate the Fréchet derivative $F'(\sigma)$ for every $\delta\sigma$. After solving two forward problems, the evaluation of $D'(\sigma)$ is a mere integration, which is especially easy for the discretized problem.